Auroral particle precipitation characterized by the substorm cycle

Simon Wing,[1] Matina Gkioulidou,[2] Jay R. Johnson,[3] Patrick T. Newell,[1] and Chih-Ping Wang[2]

Received 26 March 2012; revised 4 January 2013; accepted 13 January 2013; published 1 March 2013.

[1] Substorms release a large amount of energy, some of which is used to energize the precipitating particles in the polar region. Superposed epoch analysis was performed with 11 years of DMSP SSJ/4/5 data to characterize the substorm cycle of the diffuse, monoenergetic, and broadband/wave precipitating electrons and precipitating ions. Although substorms only increase the ion pressure by 30%, they increase the power of the diffuse, monoenergetic, and wave electron aurora by 310%, 71%, and 170%, respectively. Substorms energize the ion aurora mainly in the 21:00–05:00 magnetic local time (MLT) sector. The dynamics of the diffuse electron aurora are different from those of the other two electron aurorae. The expansion phase duration is approximately 15 min for the monoenergetic and wave electron aurorae, whereas it is 1 h for the diffuse electron aurora. The monoenergetic and wave electron aurorae appear to complete the substorm cycle within a 5 h interval, whereas the diffuse electron aurora takes more than 5 h. The diffuse electron aurora power and energy flux start increasing at 15 min before the substorm onset, whereas those for the monoenergetic and wave electron aurorae start increasing at 1 h and 15 min before the onset. The increase in the monoenergetic electron aurora power and energy flux may result from the increase in the magnetotail stretching and region-1 field-aligned current during the growth phase. The monoenergetic electrons may also be associated with fast flows, which have been previously observed more frequently in the dusk-midnight sector.

Citation: Wing, S., M. Gkioulidou, J. R. Johnson, P. T. Newell, and C.-P. Wang (2013), Auroral particle precipitation characterized by the substorm cycle, *J. Geophys. Res. Space Physics*, *118*, 1022–1039, doi:10.1002/jgra.50160.

1. Introduction

[2] A substorm is an important and common process that cycles through storing and releasing energy in the Earth's magnetosphere. Substorms occur in other planetary magnetospheres in our solar system and perhaps even in exoplanetary magnetospheres [e.g., *Mauk et al.*, 1997; *Berthomier et al.*, 2012]. There are generally three phases of a substorm: growth, expansion, and recovery. The growth phase typically begins in the quiescent period at the time of the southward turning of the interplanetary magnetic field (IMF) [e.g., *Tanskanen et al.*, 2002] and ends at the onset of the expansion phase (commonly referred to as the substorm onset). During the growth phase, the auroral oval expands equatorward, the aurora and the electrojet gradually intensify, the plasma sheet thins, and the magnetospheric magnetic field lines stretch (become tail-like), as the solar wind energy is stored in the magnetotail. The expansion phase begins at the end of the growth phase. During the expansion phase, the auroral oval brightens and expands poleward, eastward, and westward, the westward electrojet significantly increases, and the magnetic field configuration in the inner plasma sheet changes rapidly from the stretched tail-like configuration to a more dipolar configuration. The expansion phase is followed by the recovery phase, during which the magnetosphere returns back to its original undisturbed state. The start of the recovery phase is usually signaled by the waning of the substorm aurora and weakening of the westward electrojet. The recovery phase ends when the magnetosphere reaches its normal undisturbed state. A more detailed description of substorm phases can be found in *Lui* [1991].

[3] Many space phenomena or parameters cycle with the substorm cycle of growth-expansion-recovery phases. The waxing-waning of the auroral oval, the stretching-unstretching of the magnetotail, and loading-unloading of the magnetotail energy mentioned above are just a few examples of such parameters. Auroral particle precipitation is an important parameter because it provides a measure of magnetospheric energy input into the ionosphere. It can be used to indicate a state of the magnetosphere, and as such it should be affected by the substorm cycle.

[4] Using ground magnetic field observations and indices derived from these observations such as aurora electrojet

[1]Applied Physics Laboratory, The Johns Hopkins University, Laurel, Maryland, USA.
[2]Department of Atmospheric and Oceanic Sciences, University of California, Los Angeles, California, USA.
[3]Princeton Plasma Physics Laboratory, Princeton University, Princeton, New Jersey, USA.

Corresponding author: S. Wing, Applied Physics Laboratory, The Johns Hopkins University, Laurel, MD, USA. (simon.wing@jhuapl.edu)

2169-9380/13/10.1002/jgra.50160

indices, AL or AE, various studies estimated that the growth phase takes approximately 30–60 min, the expansion phase approximately 10–60 min, and the recovery phase approximately 30–120 min [e.g., *Bargatze et al*., 1999; *Horwitz*, 1985; *Pulkkinen et al*., 1994; *McPherron et al*., 1986; *Huang et al*., 2003; *Baker et al*., 1981]. Based on these estimates for the growth, expansion, and recovery phases, *Huang et al*. [2003] estimated that the complete substorm cycle takes approximately 2–3 h. In comparison, *Tanskanen et al*. [2002] reported that the average duration of the substorm, from the beginning of the growth phase to the end of the recovery phase, is approximately 4 h. They determined the substorm from a proxy for westward electroject index (AL), which is named IL index and which is derived from IMAGE data [*Kallio et al*., 2000]. However, the substorm cycle of the auroral particle precipitation is not as well known. The substorm phase durations obtained from magnetospheric particle or magnetic field observations have been found to differ from those determined from the ground magnetic field observations, AE, AL, or IL indices [e.g., *Pulkkinen et al*., 1994; *Baker et al*., 1994].

[5] *Wing et al*. [2007] presented plasma sheet pressure, temperature, and density 2D profiles for the substorm growth, expansion, early recovery, and late recovery phases. Subsequently, *Wing and Johnson* [2009] presented 2D profiles of specific entropy ($s = p/n^{\gamma}$), total entropy ($S = p^{1/\gamma}\,V$), and the total content ($N = nV$) of the plasma sheet for the same substorm phases, where p = plasma pressure, n = number density, V = flux tube volume, and γ = polytropic index. Both studies used Defense Meteorological Satellite Program (DMSP) observations to infer the plasma sheet properties. Moreover, both studies used a substorm database in which not only the onset time but also the start of the recovery phase had been carefully identified. However, the database had only 180 substorm events and as a result, some regions, particularly post-midnight, had poor data coverage.

[6] Recently, using an order of magnitude more substorm events, 4861 events, *Newell et al*. [2010] performed a superposed epoch analysis of the substorm onset to obtain statistical electron precipitation maps of wave, mono-energetic, and diffuse aurora from 4 to 6 min after substorm onset in 2 min time resolutions. These maps were obtained from DMSP SSJ/4/5 particle observations in the interval 1996–2007. These maps are quite useful in providing the global pictures of the electron precipitations minutes around the substorm onset, but they do not show the dynamics for the entire substorm cycle. *Newell et al*. [2010] also calculated the aurora power obtained by integrating the nightside auroral electron and ion precipitation from 18:00 to 06:00 magnetic local time (MLT) and from 50° to 90° magnetic latitude (MLat). These integrated auroral powers were calculated from 2 h before to 2 h after substorm onset at 2 min resolution. Unfortunately, at 2 min resolution, the statistics limit interpretation of the results and it is difficult to ascertain any trend within the substorm cycle because of large fluctuations, except at the substorm onset, when the values significantly increase. Moreover, the 2 h after onset may not be enough time to cover the entire expansion and recovery phases [e.g., *Horwitz*, 1985].

[7] The present study is an extension of the *Wing et al*. [2007], *Wing and Johnson* [2009] and *Newell et al*. [2010] studies. As in the *Newell et al*. [2010] study, the present study examines the substorm cycles in the auroral electron and ion precipitation, but on a larger time scale, covering nearly the entire substorm cycle of the electron and ion aurora. Also as in the *Newell et al*. [2010] study, the present study distinguishes three types of electrons: diffuse, wave or broadband, and monoenergetic.

[8] The diffuse aurora electrons are most likely field-aligned plasma sheet electrons that precipitate in the ionosphere. The electrons in the loss cone (the field-aligned electrons) are replenished by the pitch angle scattering resulting from electron interactions with the very low frequency (VLF) whistler-mode chorus waves [e.g., *Thorne*, 2010; *Reeves et al*., 2009; *Summers et al*., 1998]. When precipitating electrons exhibit a broad energy spectrum, they are classified as wave or broadband aurora electrons. These electrons may result from the electron interaction with the dispersive Alfvén waves [*Chaston et al*., 2002; 2003; 2008], which are often observed around the time of substorm dipolarization [*Lessard et al*., 2006]. The monoenergetic electrons, on the other hand, may indicate the presence of the parallel electric field that accelerates the electrons downward and may be associated with the evolution of the global upward current system in the plasma sheet. The monoenergetic electrons may also result from the electron interaction with low frequency Alfvén waves/ballooning modes that accelerate electrons [e.g., *Pritchett and Coroniti*, 2010; *Damiano and Johnson*, 2012]. The present study examines the characteristics and dynamics of these three types of electrons and ions throughout the substorm cycle. This can help illuminate the processes that form these electrons, the regions where they operate, and the time scales at which these processes operate within the substorm cycle. Substorm-led magnetic field dipolarization releases a large amount of energy, some of which is used to energize particle precipitation. The present study quantifies the energy gained by each type of electron during substorms. The growth phase signatures in these electrons, if there are any, should be of interest to space weather studies that aim to predict substorm onsets.

[9] Finally, the Rice Convection Model (RCM) has been used to simulate plasma transport in the magnetotail [*Toffoletto et al*., 2003]. The present study simulates the ion precipitation by using the RCM combined with a Dungey force-balanced magnetic field solver and strong diffusion. The simulation results are subsequently compared with the DMSP observations.

2. DMSP Particle Data Set

[10] Data from the SSJ/4 electrostatic analyzers on the DMSP series satellites (F12 through F15) and the SSJ/5 detector on F16 were used. The time period covered is from 1996 to 2007, although there are no onsets identified in the years 2003–2006. No DMSP F17 data were used because of uncertainties about the data quality (and F15 was used only for 2001).

[11] The DMSP satellites are in sun-synchronous, nearly circular polar orbits at approximately 845 km altitude, with orbital inclinations of 98.7°. The orbits of the DMSP satellites are such that the least covered regions are post-noon and especially post-midnight, except at high magnetic latitudes. The SSJ/4 and SSJ/5 instruments included on all these flights use curved plate electrostatic analyzers to measure electrons and ions with one complete spectrum each obtained per second.

The satellites are three-axis stabilized, and the detector apertures always point toward local zenith. At the latitudes of interest in this paper, this means that only highly field-aligned particles well within the atmospheric loss cone are observed.

3. The Substorm Database

[12] Most substorm studies determine the substorm onsets from either ground magnetic field observations (or indices derived from these observations) or from optical observations of aurora. The substorm onsets in the present study were determined from the latter. As in *Newell et al*. [2010], the present study combines two separate substorm databases: (1) the Polar UVI substorm database [*Liou et al*., 1997; 2001] and (2) the IMAGE substorm database [*Frey et al*., 2004]. There are 4861substorm events in this combined substorm data set. One difference between the present study and the *Newell et al*. [2010] study is that the present study explicitly selects only isolated substorms that are separated by at least 5 h from other substorms in this database. Of the 4861 substorm events in the original combined data set, 1677 events, or about 34%, are isolated substorms. Ideally, we would like to have more than 5 h of separation between substorms, but this would further reduce the size of the data set, which would negatively impact the statistics of the analysis. It should be noted that our selection of isolated substorms is based on observations from Polar and IMAGE, but these satellites do not cover the auroral oval continuously. Nonetheless, most of the selected substorms should still be isolated. This is because in both the Polar UVI and IMAGE substorm databases, only substorms having clear substorm onset signatures were carefully selected manually. This criterion favors isolated substorms, although not necessarily those separated by more than 5 h.

[13] The Polar UVI database was constructed from the observations of Lyman-Birge-Hopfield (LBH) bands of N_2, which are stimulated by atmospheric secondaries, and thus responsive to primary precipitating electrons above a few hundred electronvolts in energy (and ions as well, although the energy flux of the latter is typically far smaller). Although storms were not explicitly excluded, one typically cannot identify a single substorm during a storm from auroral imagery. The LBHL and LBHS filters were both used to improve time resolution. More information on the Polar UVI imager and substorm database can be found in *Liou et al*. [1997; 2001].

[14] The IMAGE substorm database was constructed from the IMAGE FUV Wideband Imaging Camera (140–180 nm) observations [*Frey et al*., 2004]. The IMAGE FUV observations are similar to the Polar UVI observations, which primarily respond to the N2 LBH lines. The selection criteria were quite similar as well. *Frey et al*. [2004] excluded substorms that occurred within 30 min of a previous onset, but in the present study, we broadened this criterion to exclude onsets that occurred within 5 h of other substorms.

4. Methodology

[15] The algorithms and method of model construction were recently described by *Newell et al*. [2009; 2010]. Here only a brief version of the approach is outlined.

4.1. Electron Aurorae

[16] The precipitating electrons are classified into three categories: diffuse, monoenergetic, and wave/broadband. Our algorithm for classifying monoenergetic electrons is as follows: (1) identifies the differential energy flux peak and subsequently looks at the drops one and two energy channels above and below the peak. If the differential energy flux drops to 30% or less of the peak within these two steps (at energies above and below the peak), then the event is considered monoenergetic. (2) The differential energy flux must be above 1.0×10^8 ($\mathrm{eV\,cm^{-2}\,s^{-1}\,sr^{-1}\,eV^{-1}}$) at the peak channel. (3) If either the average energy is below 80 eV or the differential energy flux peak is below 100 eV, the spectrum is not considered "accelerated." Such events may be spacecraft charging (some low-acceleration potentials are excluded by this rule).

[17] The algorithm for classifying wave or broadband precipitation is that if three or more energy channels have $dJ_E/dE > 2.0 \times 10^8$ ($\mathrm{eV\,cm^{-2}\,s^{-1}\,sr^{-1}\,eV^{-1}}$), an event is considered broadband. There are some caveats, which are listed in *Newell et al*. [2010] and are not repeated here.

[18] The electrons that are not classified as either broadband or monoenergetic are counted as diffuse. Hence, all electrons are classified. It has been established that both ions and electrons have a Kappa distribution in the magnetotail [*Christon et al*., 1991; *Wing and Newell*, 1998; *Kletzing et al*., 2003] and in diffuse precipitation. Although broadband and monoenergetic spectra generally drop sharply above the accelerating range, diffuse aurora may at times have a significant fraction of its energy flux outside the DMSP detector upper limit (30 keV). This is particularly true for ions, especially plasma sheet ions within 10–20 R_E, where temperatures can be 5–10 keV (recall the energy flux peaks at twice the temperature) [*Wing and Newell*, 1998; 2002]. In order to take into account the electrons having 30 keV < energy < 50 keV, for simplicity, the diffuse spectra were thus extrapolated to 50 keV, with a Maxwellian fit. This upper limit is slightly more than one additional energy channel beyond the measurements. Fitting a Maxwellian distribution requires fewer free parameters than a Kappa distribution and hence can be more robust in the cases when there are a few data points within a spectrum [e.g., *Wing and Newell*, 1998].

4.2. Ion Aurora

[19] Observationally, the signatures of the parallel electric fields and waves are less clear on ions than on electrons. It is harder to develop an automated algorithm to classify ions. Hence, we make no attempt to classify ions for the present study. The ion aurora is constructed using every spectrum, regardless of how the electron component is classified. Like the diffuse electron, ion spectra are extrapolated from the measured limit of 30 keV up to 50 keV, under the assumption that the spectra is Maxwellian, with a temperature equal to half the differential energy flux peak.

4.3. Model Construction

[20] The model resolution here is 48 MLT bins by 40 MLat bins in 15 min time steps. The analysis begins 2 h before onset and extends to 3 h after. The MLat range is 50°–90°, with data from the two hemispheres combined. Thus, although the identification of a substorm onset is nearly all from the northern

hemisphere global images, the particle precipitation maps contain roughly equal amounts of northern and southern hemispheric data. For example, a data point in the bin for 4 h after onset can also be counted in the bin for 1 h before onset.

[21] The procedure consists of analyzing every DMSP spectrum in the interval 1996–2007 and classifying the precipitation as either monoenergetic, broadband, or diffuse aurora as described in *Newell et al*. [2009; 2010], and the resulting comprehensive list of classified spectra is examined. Then the time of each spectral observation at 1 s resolution is compared with the list of substorm onsets. If the particle observation time is within 2 h before onset and 3 h after onset, it is added to the appropriate bin (determined from MLat, MLT, and time from onset). Energy and number fluxes as well as pressure are obtained from each electron and ion spectra.

[22] There are altogether approximately 3.4×10^7 spectra or points. The number of points in each bin ranges from 0 to approximately 2800. Finally, the median energy and number fluxes as well as ion pressure are computed for each bin. Auroral precipitation power in each bin is also computed by multiplying the physical surface area of each grid by the median energy flux in each bin. The auroral precipitation power is later used to compute the nightside precipitation powers as described in section 5.2. Note that our method is similar to the method used in *Newell et al*. [2010], except that they calculated the mean rather than the median in each bin. It turns out that the energy fluxes have non-Gaussian distributions. Figure 1 shows an example of an electron and an ion energy flux distribution from a randomly selected (MLat, MLT) bin. The distributions have an extended tail of high-energy fluxes that are consistent with the SME distribution, which is well correlated with Polar UVI power (see Figure 4 in *Newell and Gjerloev* [2011]). Therefore, the median would characterize a typical substorm event better than the mean, which may characterize stronger substorms.

5. Auroral Particle Precipitation Characterized by Substorm Phases

5.1. Particle Precipitation Maps Throughout the Substorm Cycle

[23] The technique used here consists of compiling electron and ion precipitation maps at 15 min cadence for 2 h before onset and 3 h after onset for each type of aurora. Figures 2–4 present diffuse, monoenergetic, and wave auroral electron energy flux maps and Figure 5 presents auroral ion energy flux map. Because of space limitation, only maps for 1 h before onset and 1 h and 45 min after onset are displayed. Figures 2–4 can be compared to Figures1–3 in *Newell et al*. [2010], which show the three kinds of precipitating electron energy fluxes, but only for several minutes before and after substorm onset. Figure 2 shows that the diffuse aurora electron energy flux increases around substorm onset, consistent with the finding in *Newell et al*. [2010]. However, Figure 2 also shows that after onset, the energy flux continues to increase and remains at an elevated level for at least 2 h after onset, reaching a maximum at about 1 h after onset (the time when the maximum is reached can be determined more easily from Figure 7, which is discussed in section 5.2). Moreover, it appears that at and after onset, the increase of the diffuse electron energy flux is confined approximately in the sector spanning 22:00–09:00 MLT.

[24] Figure 3 shows the monoenergetic auroral electron energy flux for the same interval as in Figure 2. However, its characteristics are quite different from those for the diffuse aurora. The monoenergetic aurora is concentrated mainly in the dusk-midnight sector. It appears to reach a maximum at 15 min after substorm onset. The monoenergetic aurora electron energy starts increasing approximately 1 h and 15 min before onset and increases more significantly at substorm onset. This can be more clearly seen in Figure 8 and discussed in section 5.2.

[25] Figure 4 shows the wave or broadband aurora electron energy flux from 1 h before onset to 1 h and 45 min after onset. The wave aurora rises after onset in the 21:00–02:00 MLT interval. Like the monoenergetic aurora, the wave aurora appears to wane or to start waning approximately 15 min after onset.

[26] Figure 5 shows aurora ion energy flux in the same format as Figures 2–4. Apparently, ion aurora too is enhanced after onset, but most of the enhancement occurs in the sector spanning 21:00–05:00 MLT. The enhancement appears to continue for at least 1 h and 45 min after onset as shown in Figure 5, but actually the enhancement lasts for at least 3 h after onset (not shown). *Wing et al*. [2007] and *Wing and Johnson* [2009] show that ion pressure and density increase at post-midnight in the recovery phase. Here, the pressure profile is investigated further with a database containing an order of magnitude more substorm events. Figure 6 shows the median pressure profile in the same interval as in Figures 2–5. Figure 6 shows that before the substorm onset,

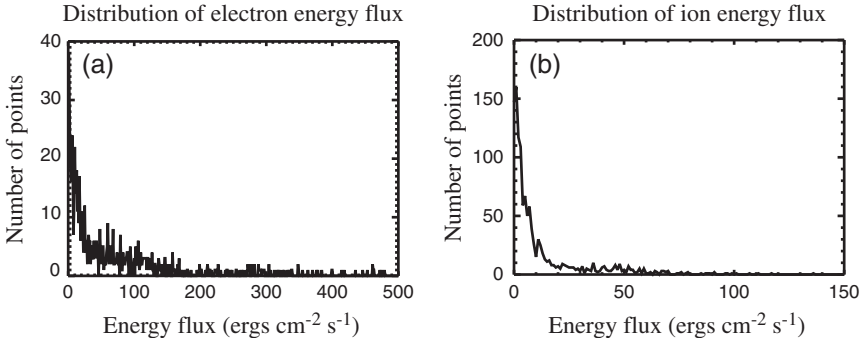

Figure 1. An example of a randomly selected (a) electron and (b) ion energy flux distribution in an (MLat, MLT) bin. Both distributions have high-energy flux tails suggesting non-Gaussian distributions.

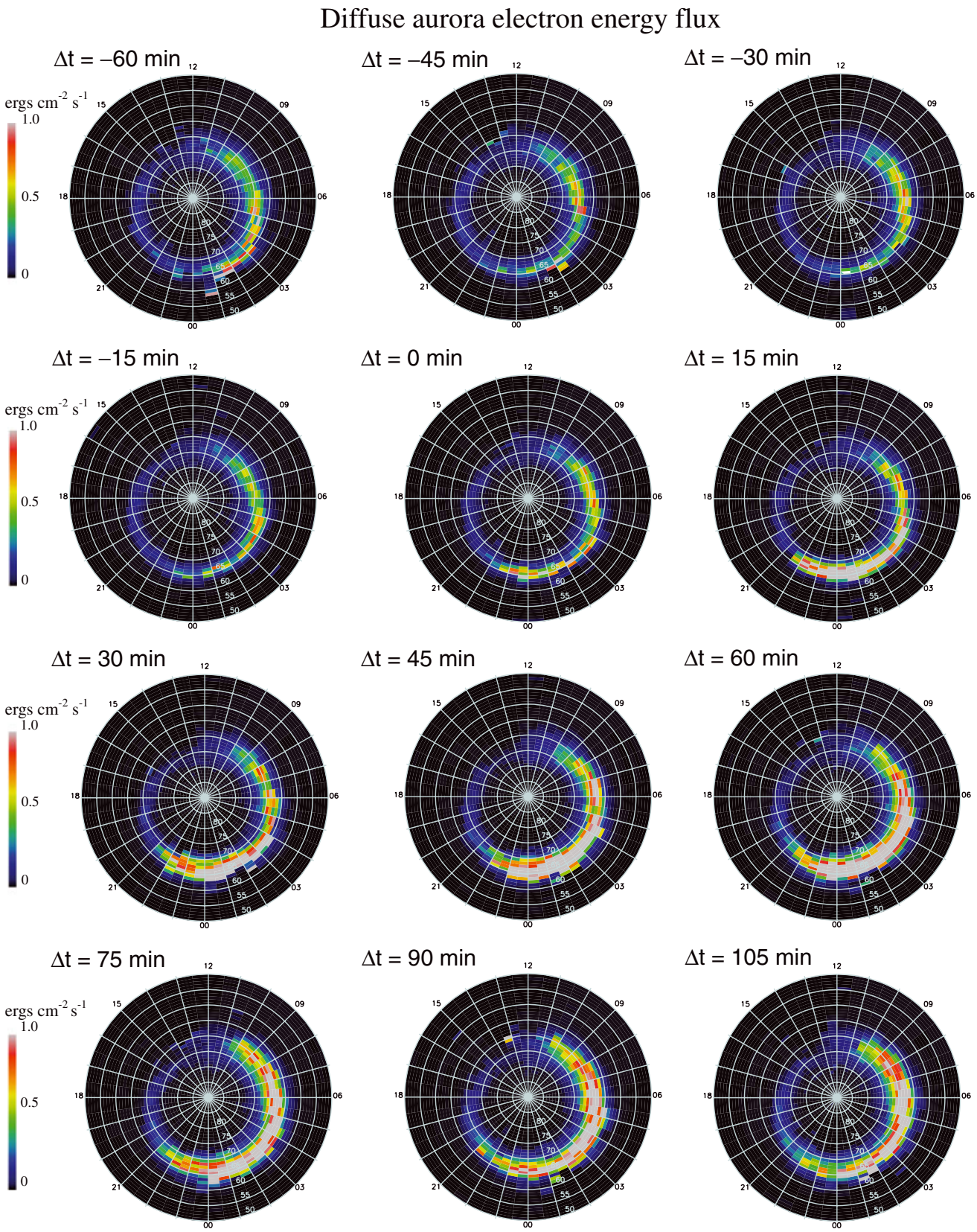

Figure 2. Diffuse aurora electron energy flux from 1 h before to 1 h and 45 min after the substorm onset. Each map shows the median energy flux over a 15 min interval centered at the time labeled. The substorm onset occurs at $\Delta t = 0$ min.

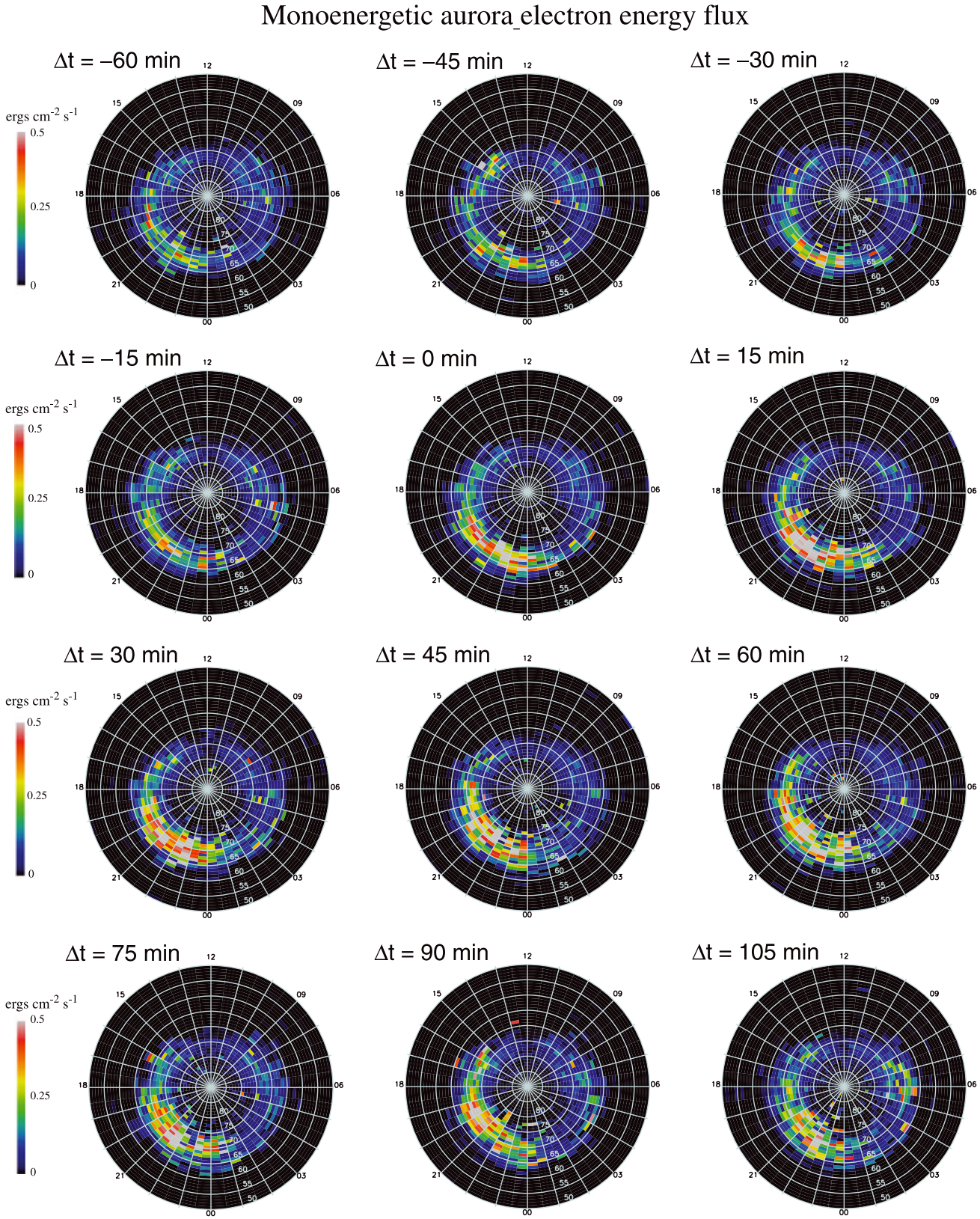

Figure 3. Monoenergetic aurora electron energy flux from 1 h before to 1 h and 45 min after the substorm onset in the same format as in Figure 2. The substorm onset occurs at $\Delta t = 0$ min.

the pressure peaks in the interval 18:00–21:00 MLT. There is a second peak at 02:00–05:00 MLT. However, after the substorm onset, the pressure increases mostly in the sector 21:00–05:00 MLT, the same local time sector where ion

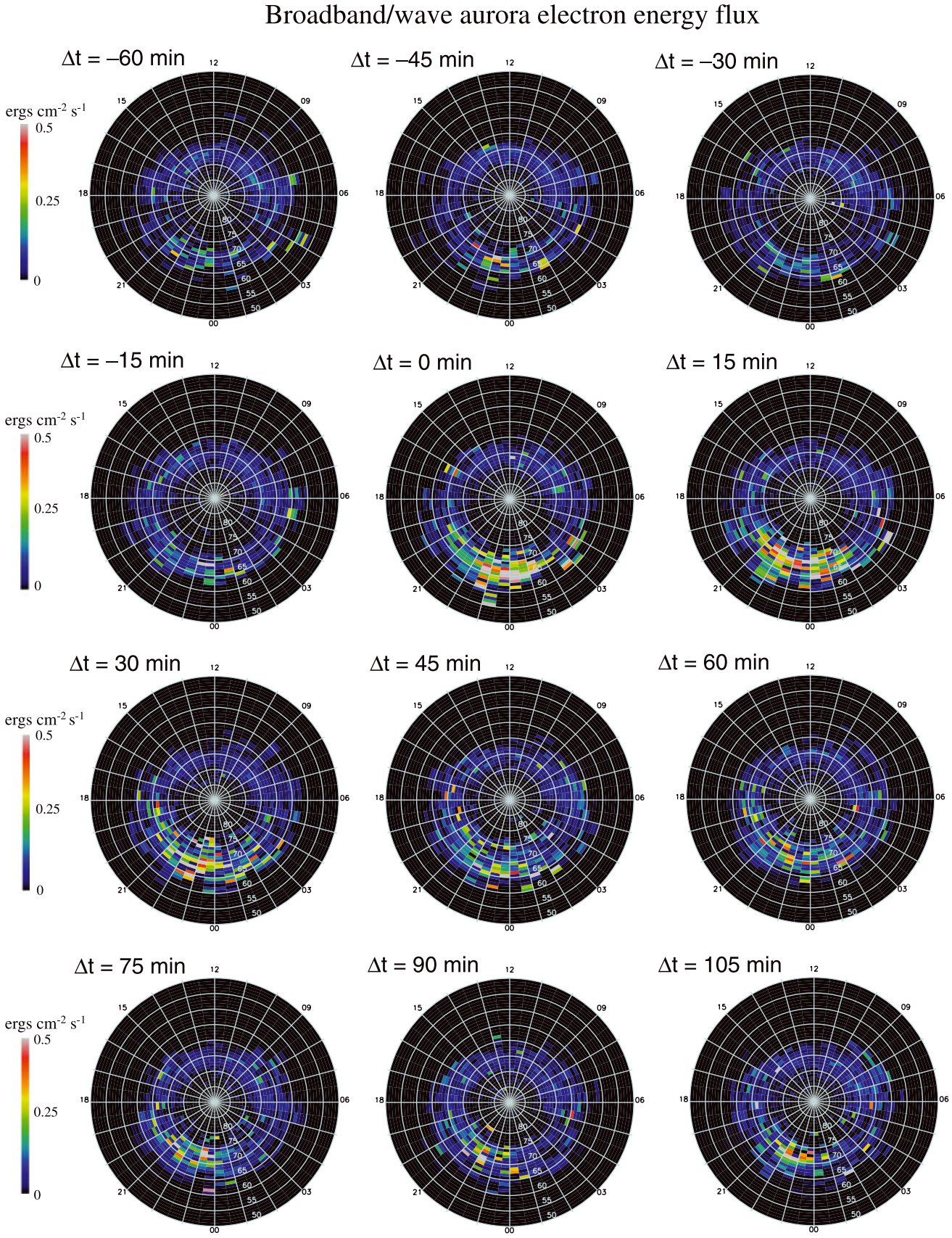

Figure 4. Broadband/wave aurora electron energy flux from 1 h before to 1 h and 45 min after the substorm onset in the same format as in Figure 2. The substorm onset occurs at $\Delta t = 0$ min.

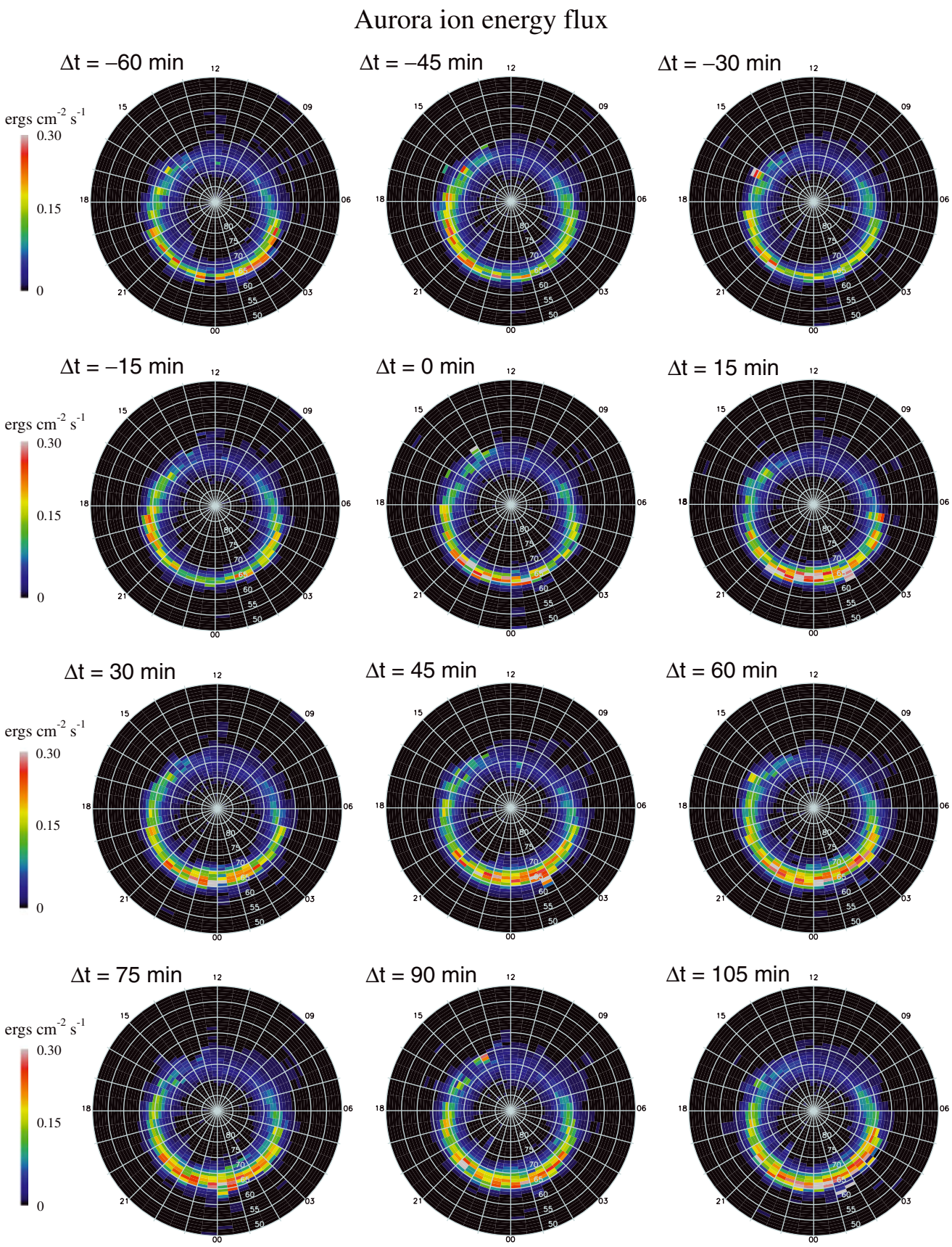

Figure 5. Aurora ion energy flux from 1 h before to 1 h and 45 min after the substorm onset in the same format as in Figure 2. The substorm onset occurs at $\Delta t = 0$ min.

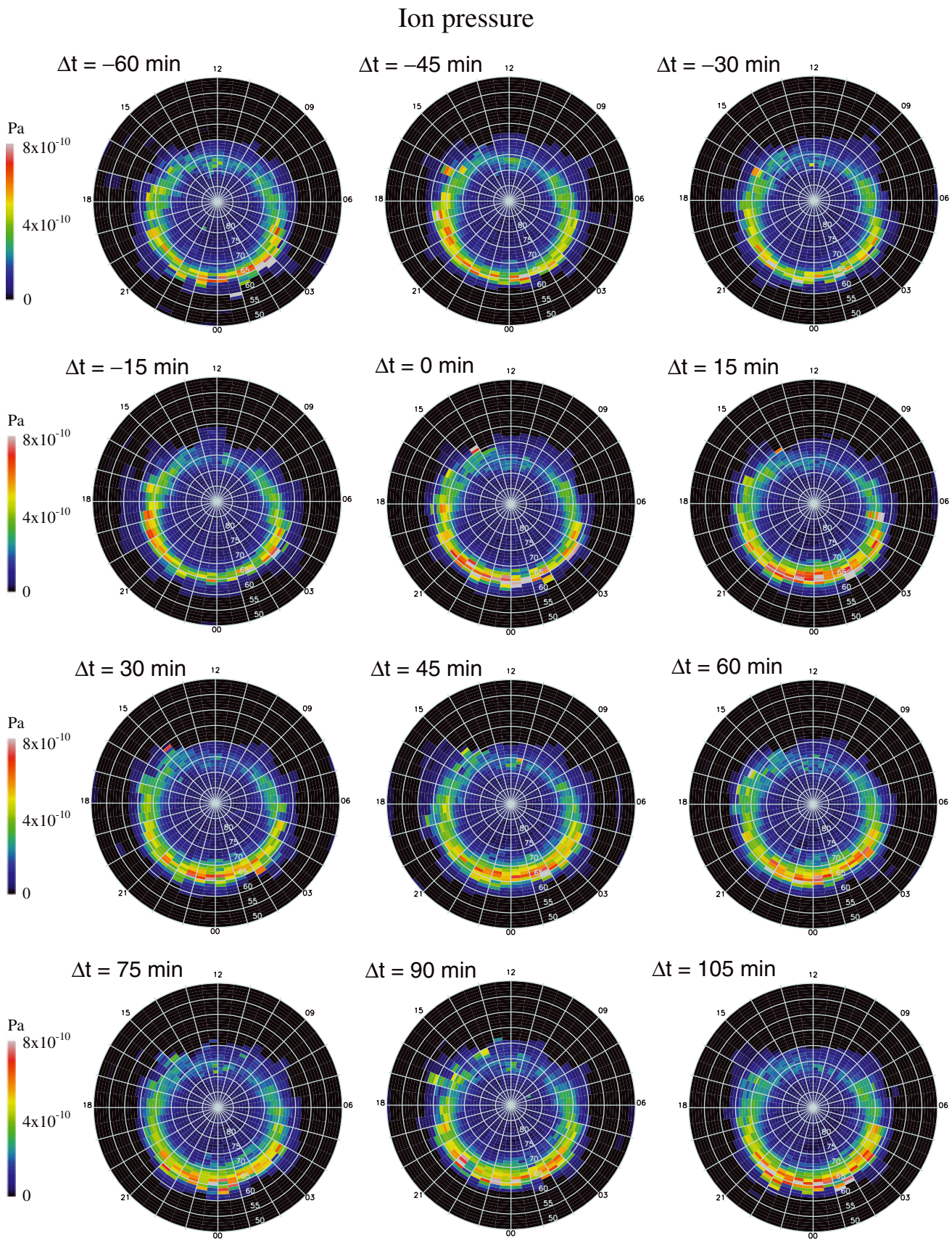

Figure 6. Ion pressure from 1 hr before to 1 h and 45 min after the substorm onset. The substorm onset occurs at $\Delta t = 0$ min.

aurora is energized, and persists for a long time, for at least 1 h and 45 min in Figure 6 (and actually longer as shown in Figure 10).

5.2. The Nightside Particle Precipitation Powers Throughout the Substorm Cycle

[27] Figures 2–6 present the particle precipitation energy flux and ion pressure maps during the substorm cycle. In this section, we examine the evolution of the nightside particle precipitation power quantitatively from 2 h before onset to 3 h after. Note that given our isolated substorm criterion (substorms are separated by more than 5 h), by restricting our analysis to 2 h before onset and 3 h after, we avoid the situation in which the same data point is counted by two bins simultaneously, by one bin before onset and one after. For example, hypothetically, a data point that fell in the bin for 4 h after onset could also fall in the bin for 1 h before onset. The dayside particle precipitation powers do not change much with substorm cycle and hence are not presented.

[28] The solid line in Figure 7 shows the diffuse electron auroral power for the entire nightside (hemispheric power). The procedure for calculating precipitation power is described in section 4.3. Each single data point on the solid line represents the integral of diffuse electron auroral powers in all bins from 18:00 to 06:00 MLT, and from 50° to 90° MLat at 15 min time resolution. So, each image in Figure 2 contributes one point on the solid line in Figure 7 and the *X* coordinate of the point corresponds to the center of the 15 min bin. The dashed line in Figure 7 plots the same thing, except it is plotted for the midnight-dawn sector, 00:00–06:00 MLT. This procedure is similar the one used in *Newell et al.* [2010].

[29] In Figure 7, the entire nightside diffuse aurora power reaches a minimum at 15 min before onset. Then, it increases at onset and continues to increase after onset, reaching a maximum at 1 h after onset. The nightside diffuse aurora power has a huge range during the substorm solar cycle, approximately 1.2 GW at 15 min before onset to 4.9 GW at about 1 h after onset. Therefore, substorm-led magnetospheric reconfiguration typically increases the diffuse aurora electron power by 310%. The error bars in Figures 6–8 are derived from the standard deviation of the median, σ_{median}, where $\sigma_{median} = 1.25\ \sigma_{dist}/\mathrm{sqrt}(N)$; σ_{dist} is the centroid 68% of the distribution, e.g., 16th–84th percentile of the distribution, and N is the number of points in the sample [e.g., *Kenney and Keeping*, 1951; *Hodges and Lehmann*, 1967]. For example, in Figure 7, the error bar $= (\sum \sigma^2_{median})^{0.5}$ of all bins in 50°–90° MLat and 18:00–06:00 MLT.

[30] The nightside diffuse electron aurora power is dominated by the power in the midnight-dawn sector. As can be seen from Figure 7, the diffuse auroral power for midnight-dawn sector (dashed line) constitutes approximately 70–80% of the power for the entire nightside (solid line).

[31] In Figure 8, the solid line plots the evolution of the nightside electron monoenergetic aurora power obtained by integrating from 18:00 to 06:00 MLT and from 50° to 90° MLat. In contrast to the diffuse aurora power, there is some indication that the monoenergetic aurora power actually starts increasing slowly at about 1 h and 15 min before onset. The monoenergetic power increases drastically at onset. After onset, the power continues to increase, but

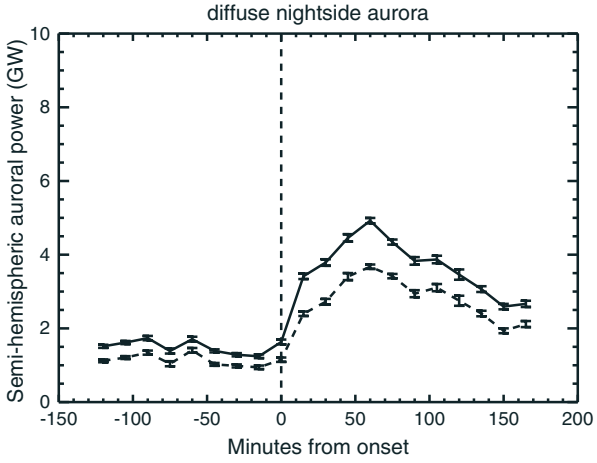

Figure 7. The nightside semi-hemispheric diffuse auroral electron power spanning the interval 2 h before to 3 h after substorm onset. The solid line shows the entire nightside power obtained from integrating the diffuse electron powers in all bins in 18:00–06:00 MLT and 50°–90° MLat. The dashed line shows the midnight-dawn powers obtained from integrating the diffuse electron power in all bins in 00:00–06:00 MLT and 50°–90° MLat. Each point in the plot is obtained from a map such as the one shown in Figure 2 (because of space limitation, Figure 2 only shows the maps for 1 h before to 1 h and 45 min after the substorm onset). The power increases sharply at substorm onset, reaching a maximum at approximately 1 h after onset. The nightside diffuse electron power comes mainly from the midnight-dawn sector.

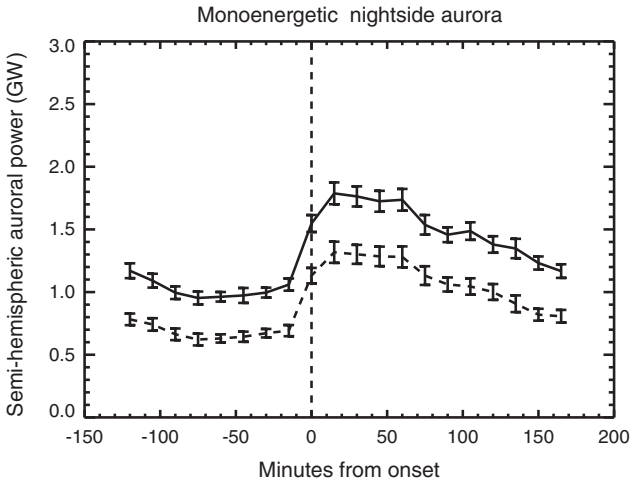

Figure 8. The nightside semi-hemispheric monoenergetic auroral electron power spanning the interval 2 h before to 3 h after substorm onset in the same format as in Figure 7. The solid line shows the power for the entire nightside obtained from integrating the monoenergetic electron powers in all bins in 18:00–06:00 MLT and 50°–90° MLat while the dashed line shows the dusk-midnight sector power obtained from integrating the powers in all bins 18:00–24:00 MLT and 50°–90° MLat. The nightside monoenergetic electron power comes mostly from the dusk-midnight sector. The power increases sharply at onset and takes approximately 3 h to return to the level at 2 h before onset. The power appears to start increasing approximately 1 h and 15 min before substorm onset.

only for a short time, reaching the maximum at 15 min after onset. The nightside monoenergetic aurora power is dominated by the power in the dusk-midnight sector, 18:00–24:00 MLT, which is plotted as the dashed line in Figure 8. From the comparison of the solid and dashed lines, it can be seen that approximately 60–75% of the monoenergetic nightside aurora power comes from the dusk-midnight sector. In other words, the power of the dusk-midnight sector is larger than that of midnight-dawn sector by approximately a factor of 1.5–3. The substorm increases the monoenergetic aurora electron power by 71% from 1.05 GW at 15 min before onset to 1.8 GW at 15 min after onset.

[32] Figure 9 plots the hemispheric nightside auroral powers for broadband or wave aurora. The solid line plots the wave aurora power integrated for the entire nightside, 18:00–06:00 MLT, whereas the dashed line plots the power integrated from 21:00 to 02:00 MLT (both are also integrated from 50° to 90° MLat). Figure 4 shows that substorms increase the wave aurora electron energy flux mainly at 21:00–02:00 MLT. Comparing the two curves in Figure 9, we can see that the power at 21:00–02:00 MLT constitutes approximately 50–75% of the total nightside power. Apparently, substorms increase the integrated power from 0.56 GW at 15 min before onset to 1.5 GW at 15 min after onset, which represents a 170% increase. Similar to monoenergetic aurora, the wave aurora peaks at 15 min after onset.

[33] Figure 10 plots the median pressure for the entire nightside from 2 h before onset to 3 h after. At each 15 min time step, the median of all the bins in 50°–90° MLat and 18:00–06:00 MLT is calculated. The error bar is σ_{median}. The median is much lower than the average pressure in the aurora oval because the median covers the region outside of the auroral oval where the pressures are lower than those within auroral oval (see Figure 6). Figure 10 shows that the pressure increases after the substorm onset and remains elevated for at least 3 h after onset relative to the value at 15 min before onset. The substorms increase the ion pressure by 30%, from 1×10^{-10} Pa at 15 min before onset to 1.3×10^{-10} Pa at 15 min after onset. The ion aurora power variation is not shown, but its variation follows roughly the same pattern as the ion pressure variation.

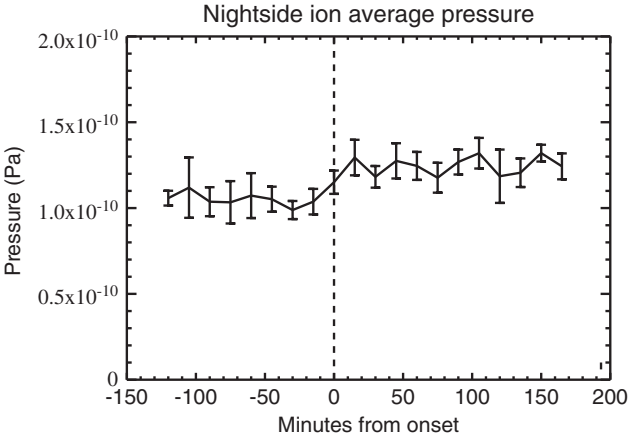

Figure 10. The nightside median ion pressure in the sector 18:00–06:00 MLT and 50°–90° MLat. The pressure increases after substorm onset and remains elevated (relative to the value at 15 min before onset) for at least 3 h. Note the pressure is low because the median is obtained from a wide latitudinal region, including the region outside the auroral oval where pressure is lower than that within the auroral oval.

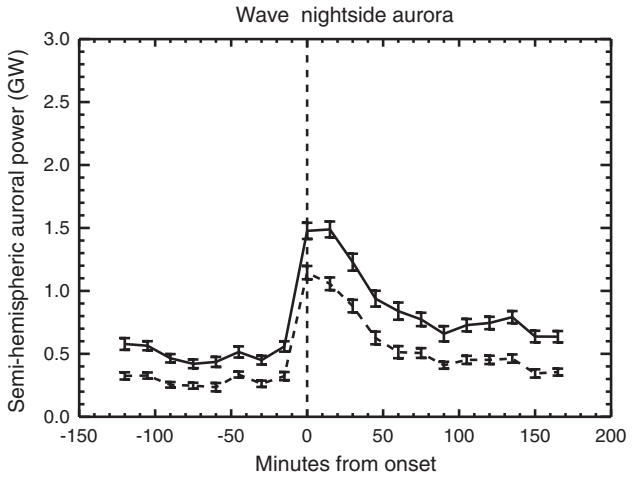

Figure 9. The nightside semi-hemispheric wave/broadband auroral electron power spanning the interval 2 h before to 3 h after substorm onset in the same format as in Figure 7. As in Figures 7 and 8, the solid line shows the power for the entire nightside obtained by integrating the wave electron powers in all bins in 18:00–06:00 MLT and 50°–90° MLat while the dashed line shows the power obtained by integrating all powers in all bins in 21:00–02:00 MLT and 50°–90° MLat. The wave electron power rises sharply at substorm onset, and reaches a maximum at 15 min after onset, but the power decreases quickly thereafter.

[34] The monoenergetic and wave electron powers complete or nearly complete the entire substorm cycle within the 5 h interval examined, 2 h before onset to 3 h after onset. That is, 3 h after onset, the powers finally reach roughly the values as those at 2 h before onset. On the other hand, the diffuse electron aurora and ion aurora powers appear to require more than 5 h to complete the cycle.

[35] The approach of quantifying the substorm effect on aurora powers is different in the present study from that of *Newell et al*. [2010] in three significant ways. First, they calculated the mean energy fluxes, instead of the median. Second, they calculated aurora powers at 2 min resolution, which shows high fluctuations perhaps due to small sampling sizes. Then, they compared the averaged powers 0–2 h before onset to those at 0–2 h after onset. As shown in Figures 7–9, the aurora powers do not vary as a step function, before and after onset, but rather they vary continuously throughout the substorm cycle, although they significantly increase around the substorm onset. Finally, not all substorms in the *Newell et al*. [2010] study are isolated substorms. In fact, 66% of their substorms are separated by less than 5 h. As a result, in the *Newell et al*. [2010] study, the same data point could be counted by a bin before onset and another bin after onset. The present study avoids this ambiguity by restricting the analysis to the interval 2 h before onset to 3 h after.

6. Comparisons of Aurora Ion Precipitation in DMSP Observations and RCM Simulation

[36] As shown in Figures 2 and 5, there are clear MLT variations in both electron and ion diffuse aurora precipitation. To investigate what processes can contribute to these MLT variations, *Gkioulidou et al*. [2012] evaluated the role of MLT-dependent electron precipitation rate by comparing the DMSP electron diffuse aurora precipitation with that from simulations of the RCM [*Toffoletto et al*., 2003] combined with a Dungey force-balanced magnetic field solver (hereafter referred to as RCM-Dungey) [*Gkioulidou et al*., 2011]. Here, we compare the DMSP ion aurora precipitation with the one obtained from the RCM-Dungey simulations with a fixed ion precipitation rate to evaluate whether the observed MLT variation can be accounted for by ion magnetic drift alone.

6.1. The RCM-Dungey Simulation

[37] The RCM-Dungey calculates the bounce-averaged electric and magnetic drift of ions and electrons assuming isotropic distributions along the magnetic field lines and slow flow approximation, within self-consistently computed electric and magnetic fields. The combined model maintains force balance in the equatorial plane. The auroral height-integrated Pedersen and Hall conductivities are estimated by the electron precipitation from the simulated plasma distributions, using the *Robinson et al*. [1987] empirical formula.

[38] *Gkioulidou et al*. [2012] conducted substorm growth phase simulations using RCM-Dungey with different electron precipitation rates and evaluated these precipitation rates by comparing the simulated precipitating electron energy fluxes with DMSP diffuse aurora electron precipitation. More specifically, they conducted simulations using six different scattering rates, which can be divided into two groups. The first group assumes the strong diffusion loss rate everywhere and two third and one third of that rate, whereas the second group assumes the MLT-dependent loss rate, based on wave activity, established by *Chen and Schulz* [2001] (hereafter referred as the Chen rate) and two third and one third of that rate. The magnitude and spatial distribution of waves vary with geomagnetic activity, but the Chen rate does not include this variability. The decisions to use the particular fractions chosen for both rates were motivated by the study of *Schumaker et al*., [1989], where data from near-geosynchronous SCATHA satellite in conjunction with polar-orbiting P78-1 revealed that the average lifetimes of plasma sheet electrons exceed those for the case of isotropy by a factor between 2 and 3 for $Kp \leq 2$ (between one half and one third of strong diffusion loss rate), and 1.5 for $Kp > 2$ (two third of strong diffusion loss rate).

[39] The location of the RCM-Dungey outer boundary is specified as a 15 R_E circle centered at $X = -5$ R_E and $Y = 0$ in the equatorial plane and reaches $X = -20$ R_E at midnight and $|Y| = 15$ R_E (on the dawn and dusk sides). The latitudes in the ionosphere that map to the outer boundary vary as the magnetic field changes. The inner boundary is at $r \sim 2$ R_E. Along the outer boundary, the proton and electron distributions at different MLT are established from a fitting of two-component Kappa distributions to statistical results of substorm growth phase periods observed by Geotail and THEMIS from 1996 to 2010. Substorm onsets were obtained from the list of *Hsu and McPherron* [2012] that is based on an appropriate change of AL. The data have been sorted into three time ranges 120–60, 60–30, and 30–0 min before the substorm onset. Only isolated substorms, i.e., those that occurred at least 3 h after the previous substorm were used. For initial plasma conditions, we use plasma distributions obtained from our previous RCM run [*Wang et al*., 2011], where we started with an empty magnetosphere and plasma from the tail boundary moved into the inner magnetosphere under many hours of enhanced convection. The boundary conditions and temporal variations of the polar cap potential drop of that previous run are shown in Figure 5 of *Wang et al*. [2011]. In this simulation, we first ran simulations with constant cross-polar-cap potential drop ($\Delta\Phi_{PC}$) of 40 kV for five simulation hours and then gradually increased $\Delta\Phi_{PC}$ to 60 kV over 2 h ($t = 5$–7 h). The magnetic field was updated every 10 min to maintain force balance with the RCM pressures. For more details on the simulation setup and the electron precipitation rates, see *Gkioulidou et al*. [2012].

[40] The investigation above showed that the simulation using a more realistic, MLT-dependent Chen rate produces electron precipitating energy flux profiles that agree better with the DMSP electron energy fluxes in their MLT distributions, compared with simulations using maximum precipitation rate against strong diffusion everywhere. In fact, using one third of the Chen rate resulted in the closest agreement between observed and simulated precipitating electron energy fluxes. Similarly, in this paper, by comparing the simulated precipitating ion energy fluxes with the observed ones from DMSP, we could determine whether the drift physics alone can account for the azimuthal distribution of the ion aurora, and also, whether assuming that ions undergo strong diffusion everywhere is a realistic approximation.

[41] Electron precipitation into the ionosphere affects the ionospheric conductance, which, in turn, affects the convection electric field and, as a result, the penetration of the ion plasma sheet into the inner magnetosphere. Therefore, because *Gkioulidou et al*. [2012] have established that using one third of the Chen electron scattering rate resulted in precipitating electron energy fluxes that were the closest to the observed ones from DMSP, in this paper we compare the DMSP ion precipitation with the simulated ion precipitation using one third of the Chen electron scattering rate.

[42] One of the main mechanisms to cause ion pitch angle scattering in the plasma sheet is the current sheet scattering [e.g., *Speiser*, 1965; *Lyons and Speiser*, 1982; *Sergeev et al*., 1983; 1993]. Ions with gyroradius comparable to or larger than the magnetic field curvature radius undergo pitch angle scattering due to violation of the first adiabatic invariant $\mu = E_{\perp}/B$. More specifically, this non-adiabatic scattering of the energetic ions happens whenever they encounter the equatorial current sheet along their orbit and provides rapid filling of the loss cone. Higher-energy ions are more likely to be scattered to the loss cone than the lower energy ones. The scattering is also expected to weaken with decreasing radial distance and from the nightside to dayside as the magnetic field lines become less stretched. Another important scattering mechanism is through interaction with electromagnetic ion cyclotron (EMIC) waves [e.g., *Jordanova et al*., 2001]. Therefore, the ion precipitation rate can vary with ion energy and location. However, unlike the location-

and energy-dependent Chen rate we used for electron precipitation in the simulation, no such ion precipitation rate has yet been established to be incorporated into our simulation. Thus, as mentioned above, we simply assumed that ions of all energies are under strong pitch angle diffusion everywhere, that is, the maximum precipitation rate for ions. This assumption is valid for the tail plasma sheet, where the ion distribution is approximately isotropic [e.g., *Stiles et al*., 1978; *Wing and Newell*, 1998; *Wing et al*., 2005], but becomes less appropriate in the inner magnetosphere (inside ~10 R_E), where the distributions can become highly anisotropic. Nevertheless, using a fixed ion precipitation rate allows us to evaluate whether magnetic drift alone can account for the MLT variations in the DMSP precipitation.

6.2. RCM Precipitating Ion Energy Flux

[43] Figure 11 shows the simulated ion precipitating energy fluxes at 6 h and 45 min of our run and the observed DMSP ion aurora precipitation 15 min before the onset (also shown in Figure 5). The RCM simulation shows that the precipitating energy flux maximizes in the dusk-midnight sector. This can be attributed to more energetic ions magnetic drifting toward dusk. DMSP observations also show a peak around 18–20 MLT. However, the simulated magnitudes are a factor of ~2 larger compared with the observed ones (please note the different color bars). This indicates that the assumed maximum ion precipitation rate overestimates the real precipitation rate.

[44] On the other hand, DMSP observations show a second peak around 02:00–05:00 MLT, which is not seen in the RCM-Dungey simulation. The pressure map also shows a second peak at the same location as can be seen in Figure 6. These ion pressure and energy flux maxima can be attributed to a peak in the ion number flux (not shown). The pressure peak around 02:00–05:00 MLT in the plasma sheet has been previously observed and attributed to a density peak during active times [e.g., *Korth et al*., 1999; *Wing and Newell*, 1998] and during growth phase [*Wing et al*., 2007; *Wing and Johnson*, 2009]. The present study obtains the same result with a larger database than the *Wing et al*. [2007] and *Wing and Johnson* [2009] studies. The dawn density enhancement during high magnetic activity may result from the cold solar wind ion entry on the dawn flank and flow stagnation when enhanced $\mathbf{E} \times \mathbf{B}$ and corotation are nearly cancelled by the curvature and gradient drifts [e.g., *Friedel et al*., 2001]. Another possible mechanism also presumes solar wind ion entry along the dawn flank, but additionally, an enhanced $\mathbf{E} \times \mathbf{B}$ pushing the solar wind origin ions closer to Earth where the flux tube volume is smaller and hence ions have higher density [*Wang et al*., 2003]. Because the maximum ion precipitation rate is used in this simulation, it is also not clear whether the relative weaker precipitation near midnight seen in observation can be a result of MLT variation in the ion precipitation rate. Figure 5 shows that the dawn peak persists after onset. This may be associated with substorm injection and flow stagnation. However, RCM does not include substorm injection physics and hence even if RCM had stagnation point, it might not show energy flux peak near dawn.

[45] In conclusion, our comparison of the MLT distributions in DMSP ion precipitating energy fluxes with a simulation taking into account drift physics reveal that the duskward magnetic drift of the more energetic ions can account for one of the two precipitation peaks, the one toward dusk. However, the simulation cannot account for the second peak, the one toward dawn, probably because of a lack of substorm injection physics or other physical processes. In addition, a more realistic ion precipitation rate should be included in a future simulation to evaluate the combined effect of magnetic drift and precipitation rate.

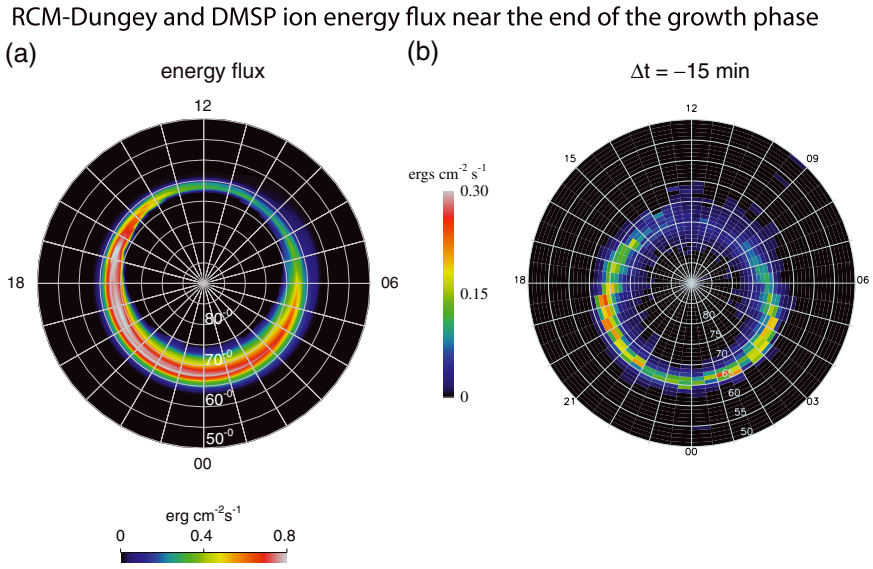

Figure 11. The precipitating ion energy flux near the end of the growth phase for (a) RCM-Dungey model and (b) DMSP observations. The RCM-Dungey ion energy flux is taken after running the simulation for 6 h and 45 min, whereas the DMSP observation is for 15 min before substorm onset (taken from Figure 5). Note that the two color bars have different scales.

7. Discussion and Summary

7.1. Summary of Key Observations

[46] Substorms change the magnetospheric configuration, e.g., when the magnetic field lines change from stretched tail-like to more dipolar configurations. During this process, a huge amount of energy is released, some of which energizes precipitating particles. On the nightside, ion and all three types of electron (diffuse, monoenergetic, and wave) energy fluxes and powers increase at or shortly after substorm onset. However, the energy increases differ for each type of aurora. The increases are 71%, 170%, and 310% for the monoenergetic, wave, and diffuse electron aurora powers, respectively. In contrast, the ion pressure increases only by 30%. Among the electron aurorae, the wave aurora has the smallest power, followed by the monoenergetic aurora, whereas the diffuse aurora has the largest power. The ion aurora power and energy flux are comparable to those of the wave electron aurora during the growth phase, but after the onset the wave electron aurora power and energy fluxes increase much more than those of the ion aurora. Substorms appear to energize ion aurora less than electron aurora of any kind.

[47] The MLT distribution of each type of aurora also differs. The diffuse electron aurora can be observed mainly in 22:00–09:00 MLT. However, the monoenergetic electron aurora power comes mainly from the dusk-midnight sector, whereas the wave aurora power comes mainly from the region centered at pre-midnight, spanning roughly 21:00 to 02:00 MLT. Near the end of the growth phase, i.e., $\Delta t = -30$ to -15 min, the ion energy flux and pressure peak at 18:00–21:00 MLT sector, which can be attributed to the ion curvature and gradient westward drifts toward dusk. There is also a second peak at 02:00–05:00 MLT in both ion energy flux and pressure maps, which can be attributed to cold solar wind ion entry along the dawn flank, flow stagnation, and enhanced $\mathbf{E} \times \mathbf{B}$ as discussed in section 6.2. After substorm onset, the ion pressure and energy flux in the 21:00–05:00 MLT sector increase and persist at an elevated level for a long time. These increases can be associated with the increase in the ion number flux (not shown). This is consistent with *Wing et al*. [2007] and *Wing and Johnson* [2009], which show that the post-midnight pressure and density increase in the recovery phase.

[48] The rest of this section examines the substorm cycle, diffuse, wave and monoenergetic electron aurorae.

7.2. Electron and Ion Aurora Substorm Cycles

[49] It is hard to determine when the growth phase begins in the particle precipitation. In the present study, the growth phase onset can be defined as the time when the power is at minimum before the substorm onset. Using this definition, the monoenergetic and wave electron aurora growth phases start at approximately 1 h and 15 min before onset. The growth phase signature for the diffuse electron aurora is not so clear. The minimum at 15 min before onset in the diffuse aurora power in Figure 7 is not likely the start of the growth phase. All types of electron and ion aurorae increase substantially at the substorm onset. So, the growth phase ends roughly at the same time for all electron and ion aurorae. In other words, the substorm onsets obtained from optical observations seem to agree with those obtained from the particle precipitation. The 1 h and 15 min duration of the growth phase for the monoenergetic and wave electron aurorae is at the upper end of the range of the growth phase obtained from ground magnetic field observations [e.g., *Bargatze et al*., 1999; *Huang et al*., 2003].

[50] The end of the expansion phase can be defined as the time when the maximum power is reached. The diffuse aurora expansion phase duration is longer than that of the other two electron aurorae. The duration of the expansion phase of the diffuse aurora is 1 h, whereas that of the monoenergetic and wave aurorae is only about 15 min. It is interesting to note that the recovery phase onset for the electron diffuse aurora, ~1 h after substorm onset, is comparable to the start of the plasma sheet recovery reported in *Baker et al*. [1994]. They reported that plasma sheet recoveries, e.g., expansion of plasma sheet, reduction of cross-tail current, etc., can occur at 10–120 min after substorm onset with a median delay of 45 min. Their substorm onsets were determined from the ground magnetic field observations. The short expansion phase duration in the electron wave aurora may result from the quick damping of the waves as discussed in section 7.4.

[51] It is a challenge to determine the end of the recovery phase, primarily because it is hard to determine when the quiet time state is reached and what the quiet time power ought to be. The quiet time power may be defined as the minimum power reached at the start of the growth phase. In Figures 7–9, it can be seen that the diffuse aurora power decreases at 1–3 h after onset, whereas the monoenergetic and wave aurora powers decrease in the interval 15 min–3 h after onset. This would suggest that the recovery phase durations are at least 2 h for the diffuse aurora and 2 h and 45 min for the monoenergetic and wave electron aurorae.

[52] For the wave and monoenergetic electron aurorae, the powers at 3 h after onset are approximately the same as those at 2 h before onset. The declining power in the interval 2–1 h before the substorm onset in the wave and monoenergetic electron aurorae may suggest that some of the points in this interval come from the recovery phase of the preceding substorm. Assuming that (1) the minimum power before the substorm onset is the baseline for the quiet time power and (2) many points in the interval 2–1 h before onset could also be in the interval 3–4 h after onset, given our criterion for isolated substorms and so the durations of the monoenergetic and wave electron aurora recovery phases can be estimated to be 3 h and 45 min or ~4 h. It is harder to determine the recovery time for the diffuse electron aurora. In the period 2–0 h before onset, the diffuse electron aurora power generally declines. Perhaps, some or many of the points in this interval may actually come from the recovery phase of the preceding substorm. This result may suggest that the recovery phase duration for the diffuse electron aurora could be more than 4 h, but in order to get a better estimate, one would have to use substorms that are separated by more than 7 or 8 h. It would not be possible to use such separations in the present dataset without severely degrading the statistics.

[53] The recovery durations of all three types of the electron precipitation are larger than the 0.5–2 h recovery duration obtained from the ground magnetic field observations [e.g., *Bargatze et al*., 1999; *McPherron et al*., 1986; *Baker et al*., 1981; *Huang et al*., 2003; *Horwitz*, 1985]. *Pulkkinen*

et al. [1994] reported that the recovery period of the geosynchronous magnetic field and energetic particle observations is on the order of 1–3 h. They attributed the long recovery of the near-Earth magnetic field to the effect of the developing ring current. However, it is not clear whether this can explain the long recovery period of the precipitating electrons, some of which map farther out than geosynchronous orbit.

[54] The duration of the substorm cycle has been reported to be approximately 2–3 h [e.g., *Huang et al*., 2003] or 4 h [e.g., *Tanskanen et al*., 2002] based on substorm onsets determined by the ground magnetic field observations or indices derived from these observations such as AE, AL, or IL. However, monoenergetic and wave electron aurora powers complete the entire substorm cycle within the 5 h interval examined. That is, 3 h after onset, the aurora powers finally reach roughly the values at 2 h before onset. The diffuse electron aurora cycle is more than 5 h. So, the durations of the substorm cycle in all electron aurorae appear larger than or at the upper end of the range of those obtained from ground magnetic field observations. These long durations can be attributed mostly to the longer durations of the recovery phases in the three types of electron aurorae.

[55] It is interesting to note that wave and monoenergetic electron aurora powers have similar substorm cycle dynamics, i.e., phases' durations, which differ from those of the electron diffuse aurora power. This is discussed further in section 7.4.

[56] The substorm energizes the precipitating ions less than the precipitating electrons. Perhaps, partly because of this, it is harder to ascertain the ion pressure cycle. The ion pressure increases only by a relatively small amount after onset, but it seems to persist at the elevated level (relative to the value 15 min before onset) for a long time. There is no clear indication that the power declines within 3 h after the substorm onset.

7.3. Diffuse Electron Aurora

[57] As shown in Figure 2, the diffuse electron aurora can be observed mainly in 22:00–09:00 MLT. The diffuse electrons are the magnetospheric field-aligned electrons that precipitate into the ionosphere. As the plasma sheet electrons $\mathbf{E} \times \mathbf{B}$ convect earthward, their curvature and gradient also drift eastward toward dawn. The field-aligned component of these electrons is quickly lost through the lost cone, but it is replenished by pitch angle scattering. A leading mechanism for pitch-angle scattering is VLF whistler-mode chorus wave-electron interactions [e.g., *Thorne*, 2010; *Reeves et al*., 2009; *Summers et al*., 1998]. Studies have shown that whistler-mode chorus waves are excited in the region spanning pre-midnight to noon, which includes the region where the diffuse electrons are observed, at 22:00–09:00 MLT. Apparently, around 09:00 MLT, the diffuse electron flux decreases, which may suggest that the whistler-mode chorus waves start weakening. In the magnetosphere, the electrons continue to drift eastward, circling the earth, but they are only observed in the ionosphere when and where there are whistler-mode chorus waves to pitch angle scatter them. The diffuse electron aurora is discussed further in the companion paper [*Gkioulidou et al*., 2012].

7.4. Wave Electron Aurora

[58] As mentioned above, substorms appear to energize wave electron aurora the most, relative to its value prior to onset. Wave aurora is characterized by precipitating electrons having a broad energy spectrum. Such precipitation is thought to result from electron interaction with dispersive Alfvén waves [*Chaston et al*., 2002, 2003, 2008]. Typical Poynting fluxes in Alfvén waves at high latitude have been shown sufficient to account for 30–35% of auroral luminosity [*Wygant et al*., 2002; *Keiling et al*., 2002]. The survey of *Chaston et al*. [2007] found that up to 40% of the total electron energy deposited in the ionosphere is associated with dispersive Alfvén waves and that an even larger fraction of energy deposition peaks in the pre-midnight region where substorms are most common.

[59] *Lessard et al*. [2006] noted a connection between dipolarization events observed in the magnetotail and dispersive Alfvén waves observed above the ionosphere, which are associated with the broadband electron precipitation. Observations of Pi1B (irregular bursty pulsations with periods from 1 to 40 s) were detected by GOES 9, FAST, and at the ground in conjunction with a substorm. While GOES detected compressional magnetic field fluctuations along with dipolarization at geosynchronous orbit, FAST (which was conjugate to GOES) detected shear Alfvén waves as a broadband ELF wave spectrum. The ratio of $\delta E/\delta B$ for the waves was consistent with Doppler-shifted dispersive Alfvén waves that have been reported [*Stasiewicz et al*., 2000; *Chaston et al*., 2008], suggesting that compressional waves mode convert to dispersive shear Alfvén waves in this region. These same waves were also observed by ground-based magnetometers on conjugate field lines.

[60] Because transfer of energy by Alfvén waves is most efficient when the perpendicular wavelength is small [*Hasegawa*, 1976; *Lysak and Song*, 2003; *Damiano et al*., 2007], it is additionally necessary that there will be a cascade of energy from large scales to small scales [*Chaston et al*., 2008]. Cross-scale coupling may result from linear phase mixing in inhomogeneity [*Lysak and Song*, 2011], nonlinear wave-wave cascade [*Schekochihin et al*., 2009 and references therein], or by nonlinear wave-particle interactions [*Damiano and Johnson*, 2012].

[61] Electrons with broadband energy distribution are consistent with acceleration in a time-varying parallel electric field [*Chaston et al*., 2002] that is associated with small-scale dispersive Alfvén waves. Electrons can be resonantly trapped in the wave potential of an Alfvén wave pulse [*Kletzing*, 1994] typically leading to the development of a velocity-dispersed beam in front of the pulse [*Watt et al*., 2005]. At lower altitude, the electrons escape the potential well and precipitate into the ionosphere as an energy-dispersed population [*Watt and Rankin*, 2009].

[62] In the transient response models [e.g., *Nishida*, 1979; *Kan et al*., 1982; *Hull et al*., 2010], the magnetospheric reconfiguration and diversion of the cross-tail currents by the current wedge are communicated to the ionosphere by Alfvén waves. The wave aurora that results from the initial substorm pulse may be expected to last a few Alfvén bounce periods because Alfvén waves damp kinetically on electrons absorbing most of the wave energy after a few reflections via wave-particle interactions [*Lysak and Song*, 2003; *Damiano*

and Johnson, 2012] and/or Joule dissipation in the ionosphere [*Hull et al*., 2010]. Wave aurora power peaks following onset and remains elevated for about 15 min, consistent with the decay time of Alfvén waves. Figure 9 shows that after the rapid decay of the main Alfvén waves in the interval 15–45 min after onset, there seems to be residual Alfvén waves that slowly decay starting at approximately 45 min after onset.

[63] Figures 7–9 suggest that wave and monoenergetic electron aurora powers have similar substorm cycle dynamics, i.e., phases' durations, which differ from those of the electron diffuse aurora power. There may be a link between wave and monoenergetic electrons. For example, recently, *Hull et al*. [2010] suggested that Alfvén waves can lead to the formation of density cavities and quasi-static parallel electric fields. However, Figures 3 and 4 show that monoenergetic and wave electrons are not always observed in the same region. They seem to overlap roughly in the region spanning 21:00–01:00 MLT. Westward of the overlapping region, e.g., MLT < 21:00, monoenergetic electrons can be observed without significant wave electrons. Conversely, eastward of the overlapping region, e.g., MLT > 01:00, wave electrons can be observed without significant monoenergetic electrons.

7.5. Monoenergetic Electron Aurora

[64] The ion and diffuse electron aurora powers and energy fluxes do not significantly increase until 0–15 min before substorm onset. However, the monoenergetic and wave electron aurora powers and energy fluxes start increasing approximately 1 h and 15 min before onset as shown in Figures 8 and 9. This suggests that any substorm prediction algorithm may do better examining the monoenergetic and wave electron aurorae than diffuse aurora.

[65] The increase of monoenergetic electron aurora about 1 h and 15 min prior to onset is suggestive of a correlation between monoenergetic electron precipitation and the growth phase magnetic field configuration. As the tail stretches during the growth phase, field-aligned currents intensify [*McPherron*, 1972; *Watanabe and Iijima*, 1993; *Wing and Sibeck*, 1997; *Tsyganenko and Sibeck*, 1994; *Tsyganenko et al*., 1993; *Zanetti and Potemra*, 1986]. In the upward field-aligned current region, the current-voltage relationship implies that the parallel potential drop would increase in order to maintain higher currents by drawing more electrons downward. Hence, an increase in the monoenergetic electron aurora may simply be an indicator of elongation of the tail that occurs during the growth phase. Figure 3 shows that the monoenergetic electrons can be observed mainly in the dusk-midnight sector. This would be consistent with the increase in the upward region-1 field-aligned current (R1) in the dusk-midnight sector during the growth phase. In the midnight-dawn sector, R1 may also increase, but here R1 is downward and so fewer monoenergetic electrons would be expected. Region-2 field-aligned current (R2) at the midnight-dawn sector also flows upward, but few monoenergetic electrons are observed at this location. This may result from the higher electron density on the dawnside than on the duskside magnetosphere due to the eastward curvature and gradient drifts of the electrons.

[66] Another possibility for the increase in monoenergetic precipitation is the development of low-frequency waves that accelerate electrons, but do not lead to global instability. One such possibility is the kinetic-ballooning/interchange mode discussed by *Pritchett and Coroniti* [2010], which operates in a stretched-tail configuration with a minimum in **B**z. These modes are thought to be associated with interchange heads, which generate auroral streamers and contribute to the monoenergetic electron precipitation. Many studies have shown that an auroral streamer is a fast-flow signature in the ionosphere [e.g., *Nakamura et al*., 2001; *Sergeev et al*., 2004]. Fast flows have been attributed to reconnection leading to flux tubes having depleted total entropy (S), which initiate unstable growth of ballooning and interchange instabilities resulting in earthward propagation of flux tubes [e.g., *Birn et al*., 2009; 2011; *McPherron et al*., 2011; *Wing and Johnson*, 2009; 2010; *Wolf et al*., 2009]. Fast flows have also been attributed to current disruption leading to field-line collapse [*Lui*, 1994; *Wolf et al*., 2009]. *Baumjohann et al*. [1999] showed that earthward fast-flow occurrence rate increases sharply about 15 min before substorm onset, consistent with the sharp increase of the nightside monoenergetic aurora power at 15 min before onset in Figure 8.

[67] Fast flows are also observed following substorm onset, in the expansion and even recovery phases. For example, *Baumjohann et al*. [1999] showed that the earthward fast flow occurrence rate peaks between 0 and 60 min after onset depending on the GSM X location of the fast flow. The superposition of these peaks may give the broad peak in the monoenergetic aurora power seen in the interval 15–60 min after onset in Figure 8. These fast flows can launch low frequency global Alfvén waves that are associated with monoenergetic precipitation [*Damiano and Johnson*, 2012]. Regardless of how they are formed, fast flows have been observed more frequently in the dusk-midnight than the midnight-dawn sector in the tail [e.g., *McPherron et al*., 2011]. This dawn-dusk asymmetry has also been seen in RCM-Equilibrium (RCM-E) simulation and has been attributed to the ion westward curvature and gradient drifts [e.g., *Zhang et al*., 2008]. We will investigate the possible links of monoenergetic electrons to fast flows and magnetic field stretching in our future studies.

[68] **Acknowledgments.** Gordon Wilson has been helpful in acquisition of DMSP SSJ/4 data, as has the World Data Center in Boulder, Colorado. Simon Wing gratefully acknowledges support from NSF grants ATM-0802715 and AGS-1058456. Matina Gkioulidou was supported by NASA grant NNX09AQ41H and NSF grant ATM-0819864. Chih-Ping Wang was supported by NASA grants NNX11AJ12G and NNX07AG42G and NSF grant ATM-0819864. Jay Johnson was funded by NASA grants (NNH09AM53I, NNH09AK63I, and NNH11AR07I), NSF grant ATM0902730, and DOE contract DE-AC02-09CH11466.

References

Baker, D. N., E. W. Hones, Jr., P. R. Higbie, and R. D. Belian (1981), Global properties of the magnetosphere during a substorm growth phase: A case study, *J. Geophys. Res.*, *86*, 8941–8956.

Baker, D. N., T. I. Pulkkinen, E. W. Hones Jr., R. D. Belian, R. L. McPherron, and V. Angelopoulos (1994), Signatures of the substorm recovery phase at high-altitude spacecraft, *J. Geophys. Res.*, *99*, 10,967-10,979.

Bargatze, L. F., T. Ogino, R. L. McPherron, and R. J. Walker (1999), Solar wind magnetic field control of magnetospheric response delay and expansion phase onset timing, *J. Geophys. Res.*, *104*, 14,583-14,599.

Baumjohann, W., M. Hesse, S. Kokubun, T. Mukai, T. Nagai, and A. A. Petrukovich (1999), Substorm dipolarization and recovery, *J. Geophys. Res.*, *104*(A11), 24,995–25,000, doi:10.1029/1999JA900282.

Berthomier, M. et al. (2012), Alfvén: Magnetosphere-ionosphere connection explorers, *Exp. Astron*, *33*, 445–489, doi:10.1007/s10686-011-9273-y.

Birn, J., M. Hesse, K. Schindler, and S. Zaharia (2009), Role of entropy in magnetotail dynamics, *J. Geophys. Res.*, *114*, A00D03, doi:10.1029/2008JA014015.

Birn, J., R. Nakamura, E. V. Panov, and M. Hesse (2011), Bursty bulk flows and dipolarization in MHD simulations of magnetotail reconnection, *J. Geophys. Res.*, *116*, A01210, doi:10.1029/2010JA016083.

Chaston, C. C., J. W. Bonnell, L. M. Peticolas, C. W. Carlson, J. P. McFadden, and R. E. Ergun (2002), Driven Alfvén waves and electron acceleration, *Geophys. Res. Lett.*, *29*, 1535.

Chaston, C. C., J. W. Bonnell, C. W. Carlson, J. P. McFadden, R. E. Ergun, and R. J. Strangeway (2003), Properties of small-scale Alfvén waves and accelerated electrons from FAST, *J. Geophys. Res.*, *108*, 8003, doi:10.1029/2002JA009420.

Chaston, C. C., C. W. Carlson, J. P. McFadden, R. E. Ergun, and R. J. Strangeway (2007), How important are dispersive Alfvén waves for auroral particle acceleration?, *Geophys. Res. Lett.*, *34*, L07101, doi:10.1029/2006JG029144.

Chaston, C., et al. (2008), Turbulent heating and cross-field transport near the magnetopause from THEMIS, *Geophys. Res. Lett.*, *35*, L17S08, doi:10.1029/2008GL033601.

Chen, M. W., and M. Schulz (2001), Simulations of diffuse aurora with plasma sheet electrons in pitch angle diffusion less than everywhere strong, *J. Geophys. Res.*, *106*(A12), 28,949–28,966, doi:10.1029/2001JA000138.

Christon, S. P., D. J. Williams, D. G. Mitchell, C. Y. Huang, and L. A. Frank (1991), Spectral characteristics of plasma sheet ion and electron populations during disturbed geomagnetic conditions, *J. Geophys. Res.*, *96*(A1), 1–22, doi:10.1029/90JA01633.

Damiano, P. A., and J. R. Johnson (2012), Electron acceleration in a geomagnetic field line resonance, *Geophys. Res. Lett.*, *39*, L02102, doi:10.1029/2011GL050264.

Damiano, P. A., A. N. Wright, R. D. Sydora, and J. C. Samson (2007), Energy dissipation via electron energization in standing shear Alfvén waves, *Phys. Plasmas*, *14*, 062,904.

Frey, H. U., S. B. Mende, V. Angelopoulos, and E. F. Donovan (2004), Substorm onset observations by IMAGE-FUV, *J. Geophys. Res.*, *109*, A10304, doi:10.1029/2004JA010607.

Friedel, R. H. W., H. Korth, M. G. Henderson, and M. F. Thomsen (2001), Plasma sheet access to the inner magnetosphere, *J. Geophys. Res.*, *106*, 5845-5858.

Gkioulidou, M., C.-P. Wang, and L. R. Lyons (2011), Effect of self-consistent magnetic field on plasma sheet penetration to the inner magnetosphere: Rice convection model simulations combined with modified Dungey force-balanced magnetic field solver, *J. Geophys. Res.*, *116*, A12213, doi:10.1029/2011JA016810.

Gkioulidou, M., C.-P. Wang, S. Wing, L. R. Lyons, R. A. Wolf, and T.-S. Hsu (2012), Effect of an MLT dependent electron loss rate on the magnetosphere-ionosphere coupling, *J. Geophys. Res.*, *117*, A11218, doi:10.1029/2012JA018032.

Hasegawa, A., Particle acceleration by MHD surface wave and formation of the aurora, *J. Geophys. Res.*, *81*, 5083, 1976.

Hodges, J. L., Jr., and E. L. Lehmann (1967), *J. Am. Stat. Ass.*, *62*(319), 926–931.

Horwitz, J. L. (1985), The substorm as an internal magnetospheric instability: Substorms and their characteristic time scales during intervals of steady interplanetary magnetic field, *J. Geophys. Res.*, *90*, 4164–4170.

Hsu, T.-S. and R. L. McPherron (2012), A statistical analysis of substorm associated tail activity, *Adv. Space Res.*, *50*(10), 1317–1343, doi:10.1016/j.asr.2012.06.034

Huang, C.-S., G. D. Reeves, J. E. Borovsky, R. M. Skoug, Z. Y. Pu, and G. Le (2003), Periodic magnetospheric substorms and their relationship with solar wind variation, *J. Geophys. Res.*, *108*(A6), 1255, doi:10.1029/2002JA009704.

Hull, A. J., M. Wilber, C. C. Chaston, J. W. Bonnell, J. P. McFadden, F. S. Mozer, M. Fillingim, and M. L. Goldstein (2010), Time development of field-aligned currents, potential drops, and plasma associated with an auroral poleward boundary intensification, *J. Geophys. Res.*, *115*, A06211, doi:10.1029/2009JA014651.

Jordanova, V. K., C. J. Farrugia, R. M. Thorne, G. V. Khazanov, G. D. Reeves, and M. F. Thomsen (2001), Modeling ring current proton precipitation by electromagnetic ion cyclotron waves during the May 14–16, 1997, storm, *J. Geophys. Res.*, *106*(A1), 7–22, doi:10.1029/2000JA002008.

Kallio, E. I., T. I. Pulkkinen, H. E. J. Koskinen, A. Viljanen, J. A. Slavin, and K. Ogilvie (2000), Loading-unloading processes in the nightside ionosphere, *Geophys. Res. Lett.*, *27*(11), 1627–1630, doi:10.1029/1999GL003694.

Kan, J. R., D. U. Longenecker, and J. V. Olson (1982), A transient response model of Pi 2 pulsations, *J. Geophys. Res.*, *87*(A9), 7483–7488, doi:10.1029/JA087iA09p07483.

Keiling, A., J. R. Wygant, C. Cattell, W. Peria, G. Parks, M. Temerin, F. S. Mozer, C. T. Russell, and C. A. Kletzing (2002), Correlation of Alfvén wave Poynting flux in the plasma sheet at 4–7 R_E with ionospheric electron energy flux, *J. Geophys. Res.*, *107*, 1132, doi:10.1029/2001JA900140.

Kenney, J. F., and E. S. Keeping (1951), Mathematics of Statistics Part Two, 2nd edition, pp. 370–371, D. V. Nostrand Co. Inc., Princeton, NJ, USA.

Kletzing, C. A. (1994), Electron acceleration by kinetic Alfvén waves, *J. Geophys. Res.*, *99*(A6), 11,095–11,103, doi:10.1029/94JA00345.

Kletzing, C. A., J. D. Scudder, E. E. Dors, and C. Curto (2003), The auroral source region: Plasma properties of the high altitude plasma sheet, *J. Geophys. Res.*, *108*, 1360, doi:10.1029/2002JA009678.

Korth, H., M. F. Thomsen, J. E. Borovsky, and D. J. McComas (1999), Plasma sheet access to geosynchronous orbit, *J. Geophys. Res.*, *104*, 25,047-25,061.

Lessard, M. R., E. J. Lund, S. L. Jones, R. L. Arnoldy, J. L. Posch, M. J. Engebretson, and K. Hayashi (2006), Nature of Pi1B pulsations as inferred from ground and satellite observations, *Geophys. Res. Lett.*, *33*, L14108, doi:10.1029/2006GL026411.

Liou, K., P. T. Newell, C.-I. Meng (1997), A. T. Y. Lui, M. Brittnacher, and G. Parks, Dayside auroral activity as a possible precursor of substorm onsets: A survey using POLAR UVI imagery, *J. Geophys. Res.*, *102*, 19835-19844.

Liou, K., P. T. Newell, D. G. Sibeck, C.-I. Meng, M. Brittnacher, and G. Parks (2001), Observation of IMF and seasonal effects in the location of auroral substorm onset, *J. Geophys. Res.*, *106*, 5799.

Lui, A. T. Y. (1991), Extended consideration of a synthesis model for magnetospheric substorms, in Magnetospheric Substorms, pp. 43-60, Geophys. Monog., 64, edited by J. R. Kan, T. A. Potemra, S. Kokubun, and T. Ijima, AGU, Washington D.C.

Lui, A. (1994), Mechanisms for the substorm current wedge, in Substorms 2: Proceedings of the Second International Conference on Substorms, Fairbanks, Alaska, March 7–11, 1994, edited by J. R. Kan, J. D. Crave, and S.-I. Akasofu, pp. 195–203, Univ. of Alaska, Fairbanks, Alaska.

Lyons, L. R. and T. W. Speiser (1982), Evidence for current sheet acceleration in the geomagnetic tail, *J. Geophys. Res.*, *87*(A4), 2276–2286, doi:10.1029/JA087iA04p02276.

Lysak, R. L., and Y. Song (2003), Kinetic theory of the Alfvén wave acceleration of auroral electrons, *J. Geophys. Res.*, *108*, 8005, doi:10.1029/2002JA009406.

Lysak, R. L., and Y. Song (2011), Development of parallel electric fields at the plasma sheet boundary layer, *J. Geophys. Res.*, *116*, A00K14, doi:10.1029/2010JA016424, [printed 117(A1), 2012].

Mauk, B. H., D. J. Williams, and R. W. McEntire (1997), Energy-time dispersed charged particle signatures of dynamic injections in Jupiter's inner magnetosphere, *Geophys. Res. Lett.*, *24*(23), 2949–2952, doi:10.1029/97GL03026.

McPherron, R. L. (1972), Substorm related changes in the geomagnetic tail: The growth phase, *Planet. Space Sci.*, *29*, 1521–1539.

McPherron, R. L., T. Terasawa, and A. Nishida (1986), Solar wind triggering of substorm expansion onset, *J. Geomag. Geoelectr*, *38*, 1089–1108.

McPherron, R. L., T.-S. Hsu, J. Kissinger, X. Chu, and V. Angelopoulos (2011), Characteristics of plasma flows at the inner edge of the plasma sheet, *J. Geophys. Res.*, *116*, A00133, doi:10.1029/2010JA015923.

Nakamura, R., W. Baumjohann, M. Brittmacher, V. A. Sergeev, M. Kubyshkina, T. Mukai, and K. Liou (2001), Flow bursts and auroral activations, *J. Geophys. Res.*, *106*(A6), 10,777–10,789.

Newell, P. T., and J. W. Gjerloev (2011), Substorm and magnetosphere characteristic scales inferred from the SuperMAG auroral electrojet indices, *J. Geophys. Res.*, *116*, A12232, doi:10.1029/2011JA016936.

Newell, P. T., T. Sotirelis, and S. Wing (2009), Diffuse, monoenergetic, and broadband aurora: The global precipitation budget, *J. Geophys. Res.*, *114*, A09207, doi:10.1029/2009JA014326.

Newell, P. T., A. R. Lee, K. Liou, S.-I. Ohtani, T. Sotirelis, and S. Wing (2010), Substorm cycle dependence of various types of aurora, *J. Geophys. Res.*, *115*, A09226, doi:10.1029/2010JA015331.

Nishida, A. (1979), Possible origin of transient dusk-to-dawn electric field in the nightside magnetosphere, *J. Geophys. Res.*, *84*(A7), 3409–3412, doi:10.1029/JA084iA07p03409.

Pritchett, P. L., and F. V. Coroniti (2010), A kinetic ballooning/interchange instability in the magnetotail, *J. Geophys. Res.*, *115*, A06301, doi:10.1029/2009JA014752.

Pulkkinen, T. I., D. N. Baker, P. K. Toivanen, R. J. Pellinen, R. H. W. Friedel, and A. Korth (1994), Magnetospheric field and current distributions during the substorm recovery phase, *J. Geophys. Res.*, *99*, 10,955-10,966.

Reeves, G. D., A. Chan, and C. Rodger (2009), New directions for radiation belt research, *Space Weather*, *7*, S07004, doi:10.1029/2008SW000436.

Robinson, R. M., R. R. Vondrak, K. Miller, T. Dabbs, and D. Hardy (1987), On calculating ionospheric conductances from the flux and energy of precipitating electrons, *J. Geophys. Res.*, *92*, 2565-2569.

Schekochihin, A. A., S. C. Cowley, W. Dorland, G. W. Hammett, G. G. Howes, E. Quataert, and T. Tatsuno (2009), Astrophysical

gyrokinetics: Kinetic and fluid turbulent cascades in magnetized weakly collisional plasmas, *Astrophys. J. Suppl. Ser.*, *182*, 310-377, doi:10.1088/0067-0049/182/1/310.

Schumaker, T. L., M. S. Gussenhoven, D. A. Hardy, and R. L. Carovillano (1989), The relationship between diffuse auroral and plasma sheet electron distributions near local midnight, *J. Geophys. Res.*, *94*(A8), 10,061–10,078, doi:10.1029/JA094iA08p10061.

Sergeev, V. A., E. M. Sazhina, N. A. Tsyganenko, J. A. Lundblad and F. Soraas (1983), Pitch-angle scattering of energetic protons in the magnetotail current sheet as the dominant source of their isotropic precipitation into the nightside ionosphere, *Planet. Space Sci.*, *31*, 1147–1155.

Sergeev, V. A., M. Malkov, and K. Mursula (1993), Testing the isotropic boundary algorithm method to evaluate the magnetic field configuration in the tail, *J. Geophys. Res.*, *98*, 7609-7620.

Sergeev, V.A., K. Liou, P. T. Newell, S.-I. Ohtani, M. R. Hairston, and F. Rich (2004), Auroral streamers: Characteristics of associated precipitation, convection and field-aligned currents, *Ann. Geophys.*, *22*, 537–548.

Speiser, T. W. (1965), Particle trajectories in model current sheets: 1. Analytical solutions, *J. Geophys. Res.*, *70*(17), 4219–4226, doi:10.1029/JZ070i017p04219.

Stasiewicz, K., et al. (2000), Small scale Alfvénic structure in the aurora, *Space Sci. Rev.*, *92*, 423.

Stiles, G. S., E. W. Hones Jr., S. J. Bame, and J. R. Asbridge (1978), Plasma sheet pressure anisotropies, *J. Geophys. Res.*, *83*(A7), 3166–3172, doi:10.1029/JA083iA07p03166.

Summers, D., R. M. Thorne, and F. Xiao (1998), Relativistic theory of wave-particle resonant diffusion with application to electron acceleration in the magnetosphere, *J. Geophys. Res.*, *103*(A9), 20,487–20,500, doi:10.1029/98JA01740.

Tanskanen, E., T. I. Pulkkinen, and H. E. J. Koskinen (2002), Substorm energy budget during low and high solar activity: 1997 and 1999 compared, *J. Geophys. Res.*, *107*(A6), 1086, 10.1029/2001JA900153.

Thorne, R. M. (2010), Radiation belt dynamics: The importance of wave-particle interactions, *Geophys. Res. Lett.*, *37*, L22107, doi:10.1029/2010GL044990.

Toffoletto, F., S. Sazykin, R. Spiro, and R. Wolf (2003), Inner magnetospheric modeling with the Rice Convection Model, *Space Sci. Rev.*, *107*, 175-196.

Tsyganenko, N. A., and D. G. Sibeck (1994), Concerning flux erosion from the dayside magnetosphere, *J. Geophys. Res.*, *99*(A7), 13,425–13,436, doi:10.1029/94JA00719.

Tsyganenko, N. A., D. P. Stern, and Z. Kaymaz (1993), Birkeland Currents in the plasma sheet, *J. Geophys. Res.*, *98*(A11), 19,455–19,464, doi:10.1029/93JA01922.

Wang, C-P, L. R. Lyons, M. W. Chen, R. A. Wolf, and F. R. Toffoletto (2003), Modeling the inner plasma sheet protons and magnetic field under enhanced convection, *J. Geophys. Res.*, *108*(A2), 1074, doi:10.1029/2002JA0009620.

Wang, C.-P., M. Gkioulidou, L. R. Lyons, R. A. Wolf, V. Angelopoulos, T. Nagai, J. M. Weygand, and A. T. Y. Lui (2011), Spatial distributions of ions and electrons from the plasma sheet to the inner magnetosphere: Comparisons between THEMIS-Geotail statistical results and the Rice convection model, *J. Geophys. Res.*, *116*, A11216, doi:10.1029/2011JA016809.

Watanabe, M., and T. Iijima (1993), Substorm growth phase on the magnetotail, *J. Geophys. Res.*, *98*(A10), 17,299–17,316, doi:10.1029/93JA01474.

Watt, C. E. J., and R. Rankin (2009), Electron trapping in shear Alfvén waves that power the aurora, *Phys. Rev. Lett.*, *102*, 045002.

Watt, C. E. J., R. Rankin, I. J. Rae, and D. M. Wright (2005), Self-consistent electron acceleration due to inertial Alfvén wave pulses, *J. Geophys. Res.*, *110*, A10S07, doi:10.1029/2004JA010877.

Wing, S., and J. R. Johnson (2009), Substorm entropies, *J. Geophys. Res.*, *114*, A00D07, doi:10.1029/2008JA013989.

Wing, S., and J. R. Johnson (2010), Introduction to special section on entropy properties and constraints related to space plasma transport, *J. Geophys. Res.*, *115*, A00D00, doi:10.1029/2009JA014911.

Wing, S., and P. T. Newell (1998), Central plasma sheet ion properties as inferred from ionospheric observations, *J. Geophys. Res.*, *103*, 6785–6800.

Wing, S., and P. T. Newell (2002), 2D plasma sheet density profile for northward and southward IMF, *Geophys. Res. Lett.*, *29*(9), doi:10.1029/2001GL013950.

Wing, S., and D. G. Sibeck (1997), The effects of interplanetary magnetic field Z-component and the solar wind dynamic pressure on the magnetospheric magnetic field line, *J. Geophys. Res.*, *102*, 7207–7216.

Wing, S., J. R. Johnson, P. T. Newell, and C.-I. Meng (2005), Dawn-dusk asymmetry in the northward IMF plasma sheet, *J. Geophys. Res.*, *110*, A08205, doi:10.1029/2005JA011086.

Wing, S., J. W. Gjerloev, J. R. Johnson, and R. A. Hoffman (2007), Substorm plasma sheet ion pressure profiles, *Geophys. Res. Lett.*, *34*, L16110, doi:10.1029/2007GL030453.

Wolf, R. A., Wan, X. Xing, J. Zhang, and S. Sazykin (2009), Entropy and plasma sheet transport, *J. Geophys. Res.*, *114*, A00D05, doi:10.1029/2009JA014044.

Wygant, J. R., et al. (2002), Evidence for kinetic Alfvén waves and parallel electron energization at 4–6 R_E altitudes in the plasma sheet boundary layer, *J. Geophys. Res.*, *107*, 1201, doi:10.1029/2001JA900113.

Zanetti, L. J., and T. Potemra (1986), The relationship of Birkeland and ionospheric current systems to the interplanetary magnetic field, in Solar Wind-Magnetosphere Coupling, edited by Y. Kamide and J. A. Slavin, pp. 547–562, Terra Sci., Tokyo.

Zhang, J.-C., R. A. Wolf, S. Sazykin, and F. R. Toffoletto (2008), Injection of a bubble into the inner magnetosphere, *Geophys. Res. Lett.*, *35*, L02110, doi:10.1029/2007GL032048.